JOURNAL OF COMPUTATIONAL PHYSICS **142,** 47–66 (1998)
ARTICLE NO. CP985921

An Accurate Second-Order Approximation Factorization Method for Time-Dependent Incompressible Navier–Stokes Equations in Spherical Polar Coordinates

Weiming Sha,* Koichi Nakabayashi,* and Hiromasa Ueda†

**Department of Mechanical Engineering, Nagoya Institute of Technology, Gokiso-Cho, Showa-Ku, Nagoya 466, Japan;†Disaster Prevention Research Institute, Kyoto University, Gokasyo, Uji City, Kyoto 611, Japan*
E-mail: sha@cfd.mech.nitech.ac.jp, nakabaya@cfd.mech.nitech.ac.jp, ueda@bouhuu.dpri.kyoto-u.ac.jp

Received July 3, 1997; revised November 11, 1997

A finite-difference method for solving three-dimensional, time-dependent incompressible Navier–Stokes equations in spherical polar coordinates is presented in detail. A new algorithm, which is second-order accurate in time and space, is considered, and decoupling between the velocity and the pressure is achieved by this algorithm. Further, the numerical method is tested by computing the spherical Couette flow between two concentric spheres with the inner one rotating. A comparison of the numerical solutions with available numerical results and experimental measurements is made. It is demonstrated that the numerical code is valid for solving three-dimensional, unsteady incompressible Navier–Stokes equations in spherical polar coordinates.

Key Words: finite-difference method; incompressible Navier–Stokes equation; spherical polar coordinate; velocity-pressure decoupling; approximation factorization method; DNS; spherical Couette flow; Taylor–Görtler (TG) vortex; spiral TG vortex.

1. INTRODUCTION

The numerical solution of the unsteady incompressible Navier–Stokes equations requires discretization in both space and time, and the discretized equations for the velocity and the pressure are a coupled system with the incompressibility condition. As these primitive variables are coupled and together they form a large system, it is very expensive to compute it directly. The coupling between the velocity and the pressure by the incompressibility constraint is one of the main concerns in designing an efficient and accurate time integration algorithm for this system.

0021-9991/98 $25.00

The split step (time splitting) method may be used as an approximation approach in which the solution of an evolution equation is advanced in time by solving a set of simple problems, each of which gives a different aspect of the physics. For solving the incompressible time-dependent Navier–Stokes equations, the pressure splitting algorithm, which was first introduced by Chorin [1], treats the pressure term and other terms separately and sequentially. Many authors developed Chorin's idea, and several versions of his algorithm have been proposed since then, e.g., the fractional step method (Kim and Moin [2]), the pressure correction method (Van Kan [3]), the projection method (Bell, Colella, and Glaz [4]; Gresho [5]). The essence of the aforementioned methods is to compute an intermediate vector field as a first step by ignoring the incompressibility constraint and then projecting the vector field onto a divergence-free field in a second step to obtain the velocity field. This decoupling process leads to several smaller decoupled systems for velocity components and the pressure, respectively, so the computational cost of calculations of the incompressible time-dependent Navier–Stokes equations can be significantly reduced in the velocity-pressure formulation. However, the above methods have two fundamental problems, i.e., subtle boundary conditions for the intermediate velocity and the pressure, and low accuracy in time integration. Fortunately, these defects were remedied recently by Dukowicz and Dvinsky [6], and Perot [7, 8]. They considered the full discretized equations in which the boundary conditions had already been applied, and therefore, no ad-hoc boundary conditions of the intermediate primitive variables were required. They also analyzed the full discretized equations with an approximate factorization method (Dukowicz and Dvinsky [6]) and a block LU decomposition method (Perot [7]), respectively, and showed the possible second or even higher order time accuracy.

Based on Dukowicz and Dvinsky's [6] approximate factorization method, a new algorithm, which is second-order accurate in time and space, will be given in this paper. Recently, some three-dimensional numerical work on the spherical Couette flow was done with a spectral method [9, 10], but there is still no literature on this work done with a finite-difference method. Here, we present a finite-difference scheme for solving the three-dimensional incompressible time-dependent Navier–Stokes equations in spherical polar coordinates. In this numerical study, the singularities of the Navier–Stokes equations in spherical polar coordinates are removed by performing spatial discretization in a semi-conservative form with the equations on a staggered grid. The spherical Couette flow between two concentric spheres is then computed with this finite-difference numerical method, and its feasibility for computing flow dynamics in spherical polar coordinates will be verified. In Section 2, the governing equations and boundary conditions are presented. The numerical method is described in detail in Section 3. In Section 4, we show some numerical results of the spherical Couette flow and a comparison with available numerical results and experimental measurements. A summary is given in Section 5.

2. GOVERNING EQUATIONS AND BOUNDARY CONDITIONS

The full incompressible Navier–Stokes equations with no body force and the continuity equation are

$$\frac{\partial \mathbf{u}}{\partial t} + \mathbf{u} \cdot \nabla \mathbf{u} = -\nabla p + \frac{1}{Re} \nabla^2 \mathbf{u}, \tag{2.1}$$

$$\nabla \cdot \mathbf{u} = 0, \tag{2.2}$$

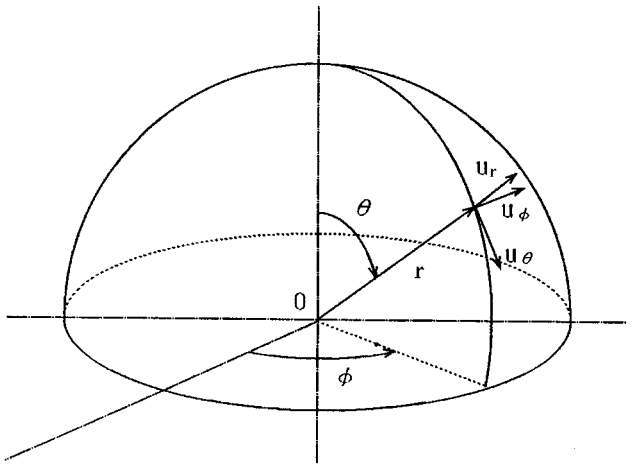

FIG. 1. Spherical Couette flow geometry.

respectively, where **u** is the velocity field, p is the kinematic pressure, and Re is the Reynolds number.

The above equations are now rewritten in a spherical polar coordinates (r, θ, φ) (see Fig. 1) as

$$\frac{\partial u_r}{\partial t} + \frac{1}{r^2}\frac{\partial}{\partial r}[r^2(u_r u_r)] + \frac{1}{r\sin\theta}\frac{\partial}{\partial\theta}[\sin\theta(u_\theta u_r)] + \frac{1}{r\sin\theta}\frac{\partial}{\partial\phi}[u_\phi u_r] - \frac{u_\theta u_\theta}{r} - \frac{u_\phi u_\phi}{r}$$
$$= -\frac{\partial p}{\partial r} + \frac{1}{Re}\left\{\frac{1}{r^2}\frac{\partial}{\partial r}\left(r^2\frac{\partial u_r}{\partial r}\right) + \frac{1}{r^2\sin\theta}\frac{\partial}{\partial\theta}\left(\sin\theta\frac{\partial u_r}{\partial\theta}\right) + \frac{1}{r^2\sin^2\theta}\frac{\partial^2 u_r}{\partial\phi^2} - \frac{2u_r}{r^2}\right.$$
$$\left. - \frac{2}{r^2\sin\theta}\frac{\partial(\sin\theta u_\theta)}{\partial\theta} - \frac{2}{r^2\sin\theta}\frac{\partial u_\phi}{\partial\phi}\right\}, \tag{2.3}$$

$$\frac{\partial u_\theta}{\partial t} + \frac{1}{r^2}\frac{\partial}{\partial r}[r^2(u_r u_\theta)] + \frac{1}{r\sin\theta}\frac{\partial}{\partial\theta}[\sin\theta(u_\theta u_\theta)] + \frac{1}{r\sin\theta}\frac{\partial}{\partial\phi}[u_\phi u_\theta] - \frac{u_\phi u_\phi}{r\tan\theta} + \frac{u_\theta u_r}{r}$$
$$= -\frac{1}{r}\frac{\partial p}{\partial\theta} + \frac{1}{Re}\left\{\frac{1}{r^2}\frac{\partial}{\partial r}\left(r^2\frac{\partial u_\theta}{\partial r}\right) + \frac{1}{r^2\sin\theta}\frac{\partial}{\partial\theta}\left(\sin\theta\frac{\partial u_\theta}{\partial\theta}\right) + \frac{1}{r^2\sin^2\theta}\frac{\partial^2 u_\theta}{\partial\phi^2}\right.$$
$$\left. + \frac{2}{r^2}\frac{\partial u_r}{\partial\theta} - \frac{u_\theta}{r^2\sin^2\theta} - \frac{2\cos\theta}{r^2\sin^2\theta}\frac{\partial u_\phi}{\partial\phi}\right\}, \tag{2.4}$$

$$\frac{\partial u_\phi}{\partial t} + \frac{1}{r^2}\frac{\partial}{\partial r}[r^2(u_r u_\phi)] + \frac{1}{r\sin\theta}\frac{\partial}{\partial\theta}[\sin\theta(u_\theta u_\phi)] + \frac{1}{r\sin\theta}\frac{\partial}{\partial\phi}[u_\phi u_\phi] + \frac{u_\phi u_r}{r} + \frac{u_\phi u_\theta}{r\tan\theta}$$
$$= -\frac{1}{r\sin\theta}\frac{\partial p}{\partial\phi} + \frac{1}{Re}\left\{\frac{1}{r^2}\frac{\partial}{\partial r}\left(r^2\frac{\partial u_\phi}{\partial r}\right) + \frac{1}{r^2\sin\theta}\frac{\partial}{\partial\theta}\left(\sin\theta\frac{\partial u_\phi}{\partial\theta}\right) + \frac{1}{r^2\sin^2\theta}\frac{\partial^2 u_\phi}{\partial\phi^2}\right.$$
$$\left. + \frac{2}{r^2\sin\theta}\frac{\partial u_r}{\partial\phi} + \frac{2\cos\theta}{r^2\sin^2\theta}\frac{\partial u_\theta}{\partial\phi} - \frac{u_\phi}{r^2\sin^2\theta}\right\}, \tag{2.5}$$

$$\frac{1}{r^2}\frac{\partial}{\partial r}(r^2 u_r) + \frac{1}{r\sin\theta}\frac{\partial}{\partial\theta}(\sin\theta u_\theta) + \frac{1}{r\sin\theta}\frac{\partial u_\phi}{\partial\phi} = 0, \tag{2.6}$$

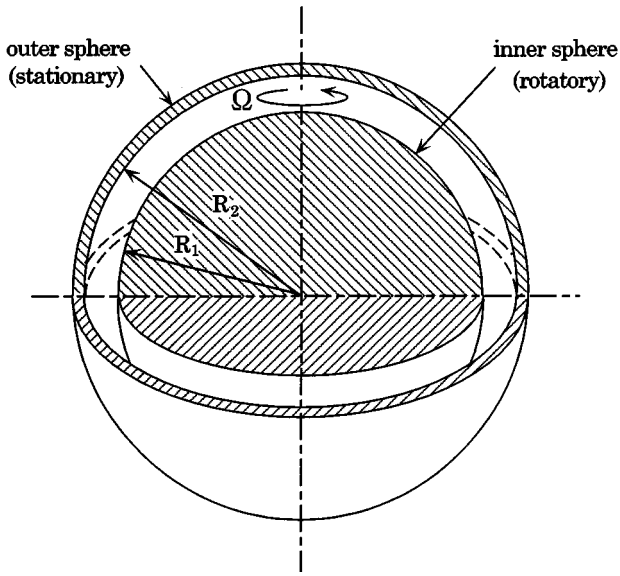

FIG. 2. Spherical polar coordinates (r, θ, ϕ) and the velocity components (u_r, u_θ, u_ϕ).

where u_r, u_θ, and u_φ are the velocity components in the radial direction, in the meridional direction, and in the circumferential direction, respectively. It can be seen that these equations are represented in a semi-conservative form.

We consider the time-dependent motion of an isothermal, incompressible, Newtonian fluid contained in an annulus between two concentric spheres (see Fig. 2). The spheres are assumed to be rigid and the cavity region between the spheres is filled with a viscous fluid. The inner sphere is constrained to rotate about the vertical axis with a prescribed angular velocity Ω, while the outer sphere is fixed. The inner and outer radii of the spheres are R_1 and R_2, respectively. The Reynolds number is defined as $Re = \Omega R_1 2/\nu$, where ν is the kinematic viscosity.

No-slip (rigid) boundary conditions on the spherical boundaries are

$$\begin{aligned} &u_r = u_\theta = 0, u_\phi = \sin\theta \quad \text{on } r = R_1/R_1 = 1, \\ &u_r = u_\theta = u_\phi = 0 \qquad\quad \text{on } r = R_2/R_1. \end{aligned} \tag{2.7}$$

3. NUMERICAL METHOD

3.1. *Temporal and Spatial Discretization in Spherical Polar Coordinates*

For brevity, we explain our discretization method with Eqs. (2.1) and (2.2), instead of the actual equations (2.3)–(2.6). Temporal and spatial discretization of Eqs. (2.1), (2.2) produces discretized equations in the form

$$\begin{aligned} &\mathbf{u}^{n+1} - \mathbf{u}^n + \frac{\Delta t}{2}[3\mathbf{H}\mathbf{u}^n - \mathbf{H}\mathbf{u}^{n-1}] \\ &\quad = -\frac{\Delta t}{2}[3\mathbf{G}p^{n+1} - \mathbf{G}p^n] + \frac{\Delta t}{2Re}[\mathbf{L}\mathbf{u}^{n+1} + \mathbf{L}\mathbf{u}^n] + \Delta t(\mathbf{mbc}), \qquad (3.1a) \\ &\qquad\qquad D\mathbf{u}^{n+1} = 0 + (\text{cbc}), \qquad (3.1b) \end{aligned}$$

where **L** is the spatially discrete Laplacian viscous term (conservative part) operator, **H** is the spatially discrete convective term plus the remaining viscous term (nonconservative

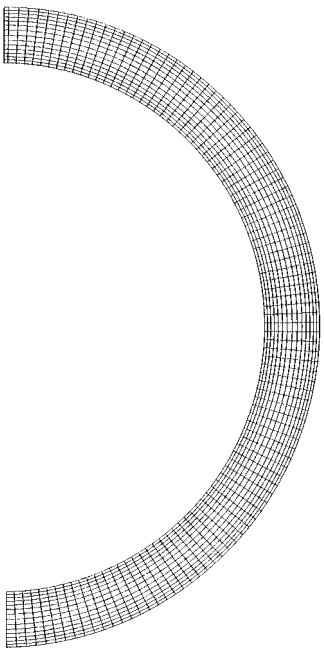

FIG. 3. Schematic computational mesh in a meridional cross section of the three-dimensional spherical shell.

part) operator, **G** is the spatially discrete gradient operator, and D is the spatially discrete divergence operator. Δt is the time increment and the superscript n means the nth time step. Space discretization is carried out in a computational domain between the two concentric spheres (see Fig. 3 for reference), and the unknown discrete variables $\mathbf{u}^{n+1}$ and p^{n+1} refer to the nodes in the interior, not to the boundary nodes. Here, the spatial discrete operators **L**, **H**, **G**, and D are evaluated using the central finite-difference scheme on a staggered grid and are second-order accurate in space. The staggered grid system used in this study will be shown concretely in Section 3.3 and Section 3.4. For the time-integration, we have used a semi-implicit time-advancement scheme with the implicit Crank–Nicolson scheme for the conservative part of the viscous term and the explicit Adams–Bashforth scheme for the convective and the remained viscous terms. The pressure term is treated in a mixed form of the Crank–Nicolson and Adams–Bashforth scheme. It is also noted that the boundary conditions for the momentum equation (**mbc**) and continuity equation (cbc) have been already incorporated in the discretized equations (3.1a), (3.1b). In the present case study, as there are clearly the periodic, homogeneous no-slip boundary conditions for the velocity, the boundary condition matrices (**mbc**) and (cbc) are identically zero (Perot [7]) and will not appear in the following section.

3.2. *Approach to the Discretized Equations (3.1a), (3.1b) with a Second-Order Approximate Factorization Method*

We can easily rewrite the discretized equations (3.1a) and (3.1b) in matrix form:

$$\begin{bmatrix} \mathbf{I} - \frac{\Delta t}{2Re}\mathbf{L} & \frac{\Delta t}{2}\mathbf{G} \\ \frac{\Delta t}{2}D & 0 \end{bmatrix} \begin{bmatrix} \mathbf{u}^{n+1} - \mathbf{u}^{n} \\ 3p^{n+1} + p^{n} \end{bmatrix} = \Delta t \begin{bmatrix} \frac{1}{Re}\mathbf{L} & \mathbf{G} \\ -\frac{1}{2}D & 0 \end{bmatrix} \begin{bmatrix} \mathbf{u}^{n} \\ p^{n} \end{bmatrix} + \Delta t \begin{bmatrix} -\frac{1}{2}(3\mathbf{H}\mathbf{u}^{n} - \mathbf{H}\mathbf{u}^{n-1}) \\ 0 \end{bmatrix}. \tag{3.2a}$$

In a manner similar to Dukowicz and Dvinsky [6], Eq. (3.2a) can be approximately factorized as

$$\begin{bmatrix} \mathbf{I} - \frac{\Delta t}{2Re}\mathbf{L} & 0 \\ 0 & \mathbf{I} \end{bmatrix} \begin{bmatrix} \mathbf{I} & \frac{\Delta t}{2}\mathbf{G} \\ \frac{\Delta t}{2}\mathrm{D} & 0 \end{bmatrix} \begin{bmatrix} \mathbf{u}^{n+1} - \mathbf{u}^n \\ 3p^{n+1} + p^n \end{bmatrix}$$

$$= \Delta t \begin{bmatrix} \frac{1}{Re}\mathbf{L} & \mathbf{G} \\ -\frac{1}{2}\mathrm{D} & 0 \end{bmatrix} \begin{bmatrix} \mathbf{u}^n \\ p^n \end{bmatrix} + \Delta t \begin{bmatrix} -\frac{1}{2}(3\mathbf{H}\mathbf{u}^n - \mathbf{H}\mathbf{u}^{n-1}) \\ 0 \end{bmatrix}. \tag{3.2b}$$

By expanding the Eq. (3.2b), we can find that it is just equivalent to

$$\mathbf{u}^{n+1} - \mathbf{u}^n + \frac{\Delta t}{2}[3\mathbf{H}\mathbf{u}^n - \mathbf{H}\mathbf{u}^{n-1}] = -\frac{\Delta t}{2}[3\mathbf{G}p^{n+1} - \mathbf{G}p^n]$$

$$+ \frac{\Delta t}{2Re}[\mathbf{L}\mathbf{u}^{n+1} + \mathbf{L}\mathbf{u}^n] + \frac{\Delta t^2}{4Re}\mathbf{L}\mathbf{G}[3\mathbf{G}p^{n+1} + \mathbf{G}p^n], \tag{3.2c}$$

$$\mathrm{D}\mathbf{u}^{n+1} = \mathbf{0}. \tag{3.2d}$$

Equations (3.2c), (3.2d) differ from Eqs. (3.1a), (3.1b) by a single additional term on the right side. It can be observed that this additional term is $O(\Delta t^3)$, and it is demonstrated that the order of the temporal accuracy is preserved. So the discretization of the method is second-order accurate in time and space.

Equation (3.2b) is exactly equivalent to the following split equations in which two new intermediate velocities $\acute{\mathbf{u}}, \grave{\mathbf{u}}$ are included:

$$\acute{\mathbf{u}} = \mathbf{u}^n + \frac{\Delta t}{2}\mathbf{G}p^n, \tag{3.2e}$$

$$\left(\mathbf{I} - \frac{\Delta t}{2Re}\mathbf{L}\right)\grave{\mathbf{u}} = \left(\mathbf{I} + \frac{\Delta t}{2Re}\mathbf{L}\right)\acute{\mathbf{u}} - \frac{\Delta t}{2}[3\mathbf{H}\mathbf{u}^n - \mathbf{H}\mathbf{u}^{n-1}], \tag{3.2f}$$

$$\mathbf{u}^{n+1} = \grave{\mathbf{u}} - \frac{3\Delta t}{2}\mathbf{G}p^{n+1}, \tag{3.2g}$$

$$\mathbf{D}\mathbf{u}^{n+1} = \mathbf{0}, \tag{3.2h}$$

Where $\mathbf{I}$ is the identity matrix. There are no boundary conditions required for the intermediate velocities as the boundary conditions have already been applied at the level of Eqs. (3.1a), (3.1b).

Taking the divergence of Eq. (3.2g) and using the incompressibility condition, Eq. (3.2h), we can obtain the following discrete Poisson equation for the pressure:

$$\frac{2}{3}\frac{\mathrm{D}\grave{\mathbf{u}}}{\Delta t} = \mathrm{D}\mathbf{G}p^{n+1} = \mathbf{L}p^{n+1}. \tag{3.2i}$$

3.3. *Method for Solving the Discrete Velocity Equation (3.2f)*

The approximate factorization technique (Beam and Warming [11]; Briley and McDonald [12]; Kim and Moin [2]) is used to treat the discrete velocity equation (3.2f). With the

definition of

$$\frac{\Delta t}{2Re}\mathbf{L} = L_r + L_\theta + L_\phi,$$

in which L_r, L_θ, and L_ϕ are the r, θ, and ϕ components of $\Delta t/(2R_e)\mathbf{L}$, respectively, we rewrite Eq. (3.2f) as

$$(\mathbf{I} - L_r - L_\theta - L_\phi)(\grave{\mathbf{u}} - \acute{\mathbf{u}}) = 2(L_r + L_\theta + L_\phi)\acute{\mathbf{u}} - \frac{\Delta t}{2}(3\mathbf{H}\mathbf{u}^n - \mathbf{H}\mathbf{u}^{n-1}). \quad (3.3a)$$

Equation (3.3a) can be factorized as

$$(\mathbf{I} - L_r)(\mathbf{I} - L_\theta)(\mathbf{I} - L_\phi)(\grave{\mathbf{u}} - \acute{\mathbf{u}}) = 2(L_r + L_\theta + L_\phi)\acute{\mathbf{u}} - \frac{\Delta t}{2}(3\mathbf{H}\mathbf{u}^n - \mathbf{H}\mathbf{u}^{n-1}). \quad (3.3b)$$

It is easy to show that the above approximation of Eq. (3.3a) is of order $O(\Delta t^3)$.

As the discrete operators L_r, L_θ, L_ϕ and $\mathbf{H}$ act on a staggered grid (see Fig. 4), the treatment of the singularities in the original equations is then simplified. Further, L_r**(ù-ú)**, L_θ**(ù-ú)**, and L_ϕ**(ù-ú)** can be expressed with the replacement of **(ù-ú)** $= (u_1, u_2, u_3)$ as

$$\begin{aligned}
L_r u_1 &= \frac{\Delta t}{2Re}\frac{1}{r^2(i)}\frac{1}{r\left(i+\frac{3}{2}\right) - r\left(i+\frac{1}{2}\right)} \\
&\quad \times \left[r^2\left(i+\frac{3}{2}\right)\frac{u_1(i+1) - u_1(i)}{r(i+1) - r(i)} - r^2\left(i+\frac{1}{2}\right)\frac{u_1(i) - u_1(i-1)}{r(i) - r(i-1)}\right], \\
L_\theta u_1 &= \frac{\Delta t}{2Re}\frac{1}{r^2(i)}\frac{1}{\sin\theta\left(k-\frac{1}{2}\right)}\frac{1}{\Delta\theta} \\
&\quad \times \left[\sin\theta(k)\frac{u_1(k+1) - u_1(k)}{\Delta\theta} - \sin\theta(k-1)\frac{u_1(k) - u_1(k-1)}{\Delta\theta}\right], \\
L_\phi u_1 &= \frac{\Delta t}{2Re}\frac{1}{r^2(i)}\frac{1}{\sin^2\theta\left(k-\frac{1}{2}\right)}\left[\frac{u_1(j+1) - 2u_1(j) + u_1(j-1)}{(\Delta\phi)^2}\right]
\end{aligned}$$

in the radial direction,

$$\begin{aligned}
L_r u_2 &= \frac{\Delta t}{2Re}\frac{1}{r^2\left(i+\frac{1}{2}\right)}\frac{1}{r(i) - r(i-1)} \\
&\quad \times \left[r^2(i)\frac{u_2(i+1) - u_2(i)}{r\left(i+\frac{3}{2}\right) - r\left(i+\frac{1}{2}\right)} - r^2\left(i-\frac{1}{2}\right)\frac{u_2(i) - u_2(i-1)}{r\left(i+\frac{1}{2}\right) - r\left(i-\frac{1}{2}\right)}\right], \\
L_\theta u_2 &= \frac{\Delta t}{2Re}\frac{1}{r^2\left(i+\frac{1}{2}\right)}\frac{1}{\sin\theta(k)}\frac{1}{\Delta\theta} \\
&\quad \times \left[\sin\theta\left(k+\frac{1}{2}\right)\frac{u_2(k+1) - u_2(k)}{\Delta\theta} - \sin\theta\left(k-\frac{1}{2}\right)\frac{u_2(k) - u_2(k-1)}{\Delta\theta}\right], \\
L_\phi u_2 &= \frac{\Delta t}{2Re}\frac{1}{r^2\left(i+\frac{1}{2}\right)}\frac{1}{\sin^2\theta(k)}\left[\frac{u_2(j+1) - 2u_2(j) + u_2(j-1)}{(\Delta\phi)^2}\right]
\end{aligned}$$

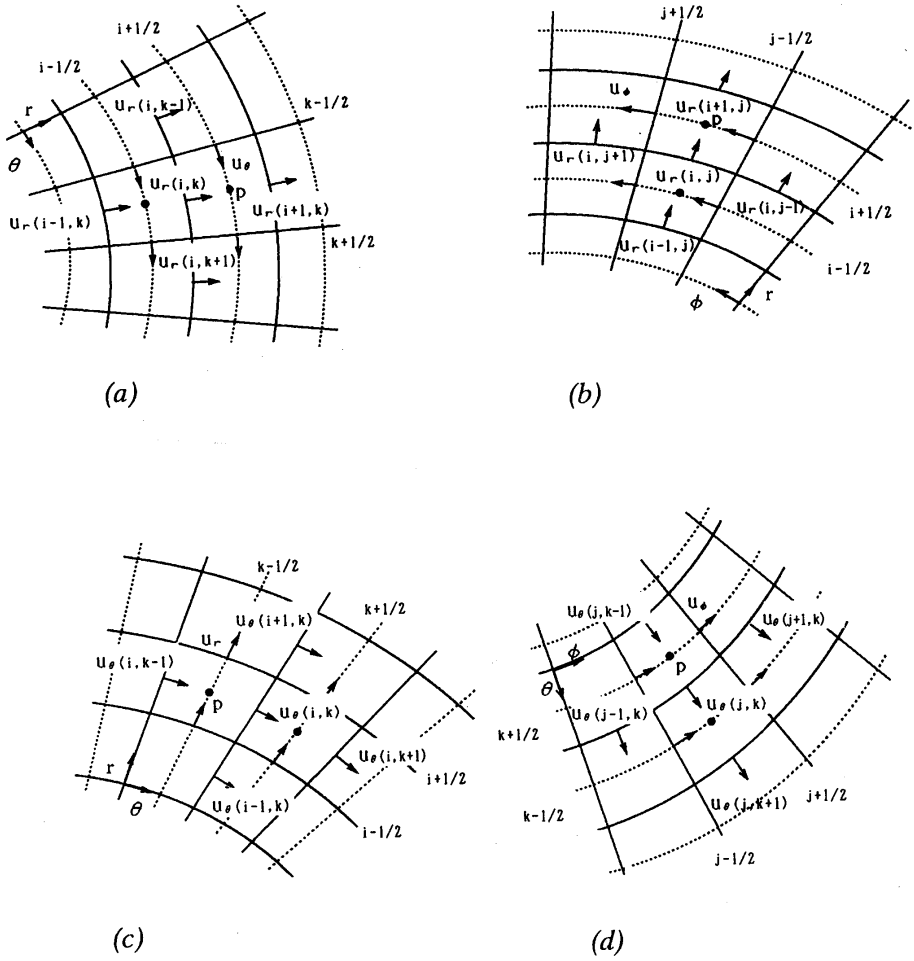

FIG. 4. Staggered grid system used for the velocities: (a) for computing the radial velocity on meridional plane (r, θ); (b) for the same as (a) but on circumferential plane (r, ϕ); (c) for computing the meridional velocity on meridional plane (r, θ); (d) for the same as (c) but on plane (θ, ϕ); (e) for computing the circumferential velocity on circumferential plane (r, ϕ); (f) for the same as (e) but on plane (θ, ϕ).

in the meridional direction, and

$$L_r u_3 = \frac{\Delta t}{2Re}\frac{1}{r^2\left(i+\frac{1}{2}\right)}\frac{1}{r(i)-r(i-1)} \times \left[r^2(i)\frac{u_3(i+1)-u_3(i)}{r\left(i+\frac{3}{2}\right)-r\left(i+\frac{1}{2}\right)} - r^2(i-1)\frac{u_3(i)-u_3(i-1)}{r\left(i+\frac{1}{2}\right)-r\left(i-\frac{1}{2}\right)}\right],$$

$$L_\theta u_3 = \frac{\Delta t}{2Re}\frac{1}{r^2\left(i+\frac{1}{2}\right)}\frac{1}{\sin\theta\left(k-\frac{1}{2}\right)}\frac{1}{\Delta\theta} \times \left[\sin\theta(k)\frac{u_3(k+1)-u_3(k)}{\Delta\theta} - \sin\theta(k-1)\frac{u_2(k)-u_2(k-1)}{\Delta\theta}\right],$$

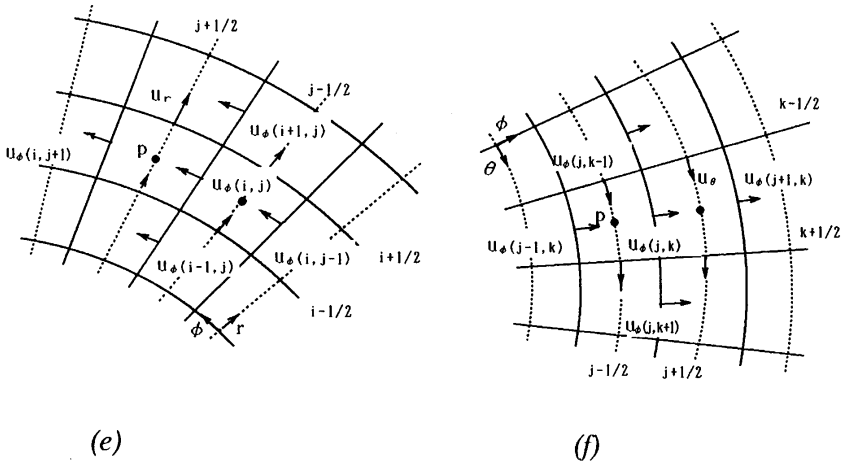

FIG. 4—*Continued*

$$L_\phi u_3 = \frac{\Delta t}{2Re}\frac{1}{r^2\left(i+\frac{1}{2}\right)}\frac{1}{\sin^2\theta\left(k-\frac{1}{2}\right)}\left[\frac{u_2(j+1)-2u_2(j)+u_2(j-1)}{(\Delta\phi)^2}\right]$$

in the circumferential direction, where $\Delta\theta$ and $\Delta\phi$ are uniform increments in the meridional direction and in the circumferential direction, respectively. We compute the discrete velocity of Eq. (3.3b) by solving three tridiagonal matrices with a standard TDMA (tridiagonal-matrix algorithm) method.

3.4. *Method for Solving the Discrete Poisson Equation (3.2i)*

We multiply the discrete Poisson equation (3.2i) by $(r\sin\theta)^2(i,k)$, and then represent it definitely on a MAC staggered grid (Harlow and Welch [13]; see Fig. 5) as

$$\begin{aligned}
&\frac{\sin^2\theta(k)}{r\left(i+\frac{1}{2}\right)-r\left(i-\frac{1}{2}\right)}\left[r^2\left(i+\frac{1}{2}\right)\frac{p^{n+1}(i+1,j,k)-p^{n+1}(i,j,k)}{r(i+1)-r(i)}\right.\\
&\left.-r^2\left(i-\frac{1}{2}\right)\frac{p^{n+1}(i,j,k)-p^{n+1}(i-1,j,k)}{r(i)-r(i-1)}\right]\\
&+\frac{\sin\theta(k)}{\Delta\theta}\left[\sin\theta\left(k+\frac{1}{2}\right)\frac{p^{n+1}(i,j,k+1)-p^{n+1}(i,j,k)}{\Delta\theta}\right.\\
&\left.-\sin\theta\left(k-\frac{1}{2}\right)\frac{p^{n+1}(i,j,k)-p^{n+1}(i,j,k-1)}{\Delta\theta}\right]\\
&+\frac{p^{n+1}(i,j+1,k)-2p^{n+1}(i,j,k)+p^{n+1}(i,j-1,k)}{\Delta\phi^2}\\
&\quad=\frac{2}{3}(r\sin\theta)^2(i,k)\frac{D\mathbf{\grave{u}}}{\Delta t}.
\end{aligned}\tag{3.4a}$$

Rearranging the Eq. (3.4a) gives

$$S(i,k)p^{n+1}(i,j,k)=A_{+1}(i,k)p^{n+1}(i+1,j,k)+A_{-1}(i,k)p^{n+1}(i-1,j,k)$$

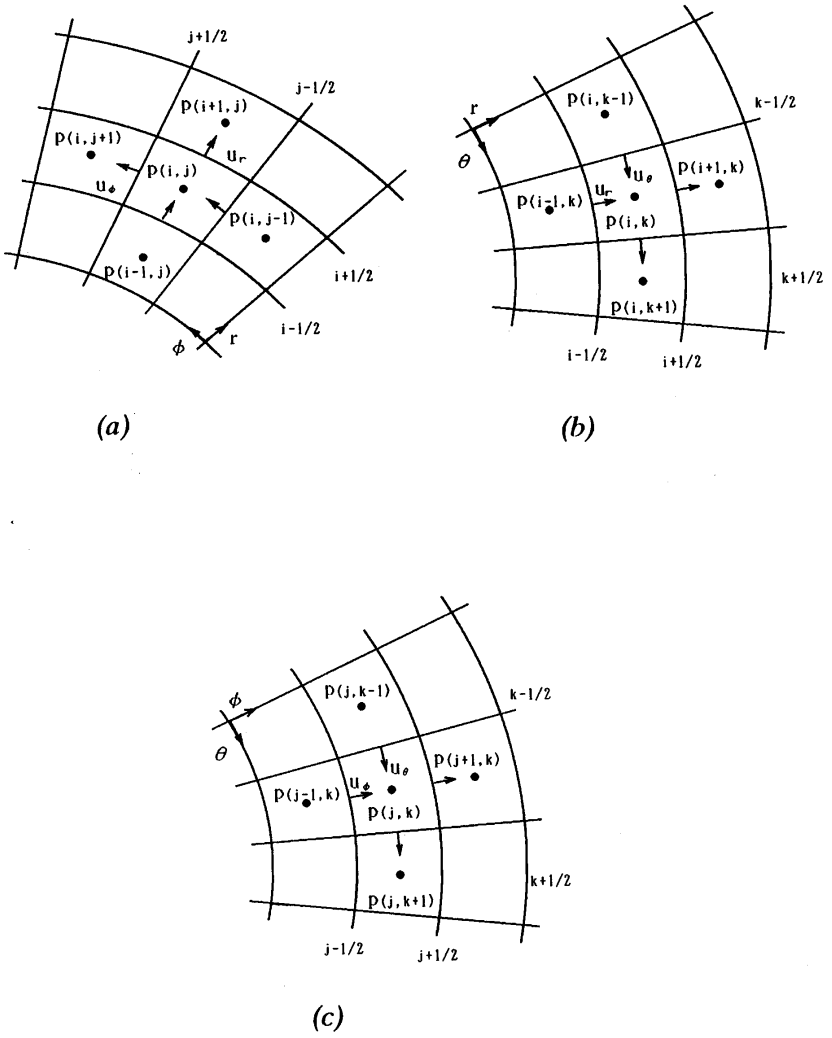

FIG. 5. Staggered grid system used for the pressure: (a) for computing the pressure on meridional plane (r, θ); (b) for the same as (a) but on circumferential plane (r, θ); (c) for the same as (a) but on plane (θ, ϕ).

$$+ \mathrm{B}\{\mathrm{p}^{n+1}(\mathrm{i}, \mathrm{j}+1, \mathrm{k}) + \mathrm{p}^{n+1}(\mathrm{i}, \mathrm{j}-1, \mathrm{k})\}$$

$$+ \mathrm{C}_{+1}(\mathrm{k})\mathrm{p}^{n+1}(\mathrm{i}, \mathrm{j}, \mathrm{k}+1) + \mathrm{C}_{-1}(\mathrm{k})\mathrm{p}^{n+1}(\mathrm{i}, \mathrm{j}, \mathrm{k}-1)$$

$$- \frac{2}{3}(\mathrm{r}\sin\theta)^2(\mathrm{i}, \mathrm{k})\mathrm{D}\dot{\mathbf{u}}. \tag{3.4b}$$

Here,

$$\mathrm{S}(\mathrm{i}, \mathrm{k}) = \mathrm{A}_{+1}(\mathrm{i}, \mathrm{k}) + \mathrm{A}_{-1}(\mathrm{i}, \mathrm{k}) + 2\mathrm{B} + \mathrm{C}_{+1}(\mathrm{k}) + \mathrm{C}_{-1}(\mathrm{k}), \quad \mathrm{B} = \frac{\Delta \mathrm{t}}{(\Delta\phi)^2},$$

$$\mathrm{A}_{+1}(\mathrm{i}, \mathrm{k}) = \Delta \mathrm{t}\frac{\mathrm{r}^2\left(\mathrm{i}+\frac{1}{2}\right)\sin^2\theta(\mathrm{k})}{\left[\mathrm{r}\left(\mathrm{i}+\frac{1}{2}\right) - \mathrm{r}\left(\mathrm{i}-\frac{1}{2}\right)\right][\mathrm{r}(\mathrm{i}+1) - \mathrm{r}(\mathrm{i})]},$$

$$A_{-1}(i,k) = \Delta t \frac{r^2\left(i-\frac{1}{2}\right)\sin^2\theta(k)}{\left[r\left(i+\frac{1}{2}\right)-r\left(i-\frac{1}{2}\right)\right][r(i)-r(i-1)]},$$

$$C_{+1}(k) = \frac{\Delta t}{(\Delta\theta)^2}\sin\theta(k)\sin\theta\left(k+\frac{1}{2}\right), \quad C_{+1}(k) = \frac{\Delta t}{(\Delta\theta)^2}\sin\theta(k)\sin\theta\left(k-\frac{1}{2}\right),$$

$$(r\sin\theta)^2(i,k)D\dot{\mathbf{u}} = (\sin^2\theta)(k)\left\{\frac{[r^2\dot{u}_r]\left(i+\frac{1}{2}\right)-[r^2\dot{u}_r]\left(i-\frac{1}{2}\right)}{r\left(i+\frac{1}{2}\right)-r\left(i-\frac{1}{2}\right)}\right\}$$

$$+ r(i)(\sin\theta)(k)\left\{\frac{\sin\theta\left(k+\frac{1}{2}\right)\dot{u}_\theta\left(k+\frac{1}{2}\right)-\sin\theta\left(k-\frac{1}{2}\right)\dot{u}_\theta\left(k-\frac{1}{2}\right)}{\Delta\theta}\right\}$$

$$+ r(i)\sin\theta(k)\left\{\frac{\dot{u}_\phi\left(j+\frac{1}{2}\right)-\dot{u}_\phi\left(j-\frac{1}{2}\right)}{\Delta\phi}\right\}.$$

The discretized equations, (3.4a) and (3.4b), are the ones for the grids not adjacent to the boundaries. For the grids adjacent to the boundaries, these equations are modified as the velocity boundary conditions are incorporated. For example, for the grids adjacent to the boundaries in radial and meridional directions ($i = 2, k = 2$), we have the following equation from (3.4a):

$$\frac{\sin^2\theta(2)}{r\left(\frac{5}{2}\right)-r\left(\frac{3}{2}\right)}\left[r^2\left(\frac{5}{2}\right)\frac{p^{n+1}(3)-p^{n+1}(2)}{r(3)-r(2)} - r^2\left(\frac{3}{2}\right)\left(\frac{\Delta p^{n+1}}{\Delta r}\right)(2)\right]$$

$$+ \frac{\sin\theta(2)}{\Delta\theta}\left[\sin\theta\left(\frac{5}{2}\right)\frac{p^{n+1}(3)-p^{n+1}(2)}{\Delta\theta} - \sin\theta\left(\frac{3}{2}\right)\left(\frac{\Delta p^{n+1}}{\Delta\theta}\right)(2)\right]$$

$$+ \frac{p^{n+1}(j+1)-2p^{n+1}(j)+p^{n+1}(j-1)}{\Delta\phi^2} = \frac{2}{3}(r\sin\theta)^2(2,2)\frac{D\dot{\mathbf{u}}(2,2,j)}{\Delta t}. \quad (3.4c)$$

Next, we consider the discrete equation (3.2g) with the velocity conditions at the boundaries, e.g.,

$$\left(\frac{\Delta p^{n+1}}{\Delta r}\right)(2) = -\frac{2}{3}\frac{1}{\Delta t}\left(u_r^{n+1}-\dot{u}_r\right)\Big|_{\text{wall}} = 0$$

in radial direction and

$$\left(\frac{\Delta p^{n+1}}{\Delta\theta}\right)(2) = -\frac{2}{3}\frac{r(i)}{\Delta t}\left(u_\theta^{n+1}-\dot{u}_\theta\right)\Big|_{\text{wall}} = 0$$

in meridional direction.

These relations are the Neumann boundary conditions and are consistent with the specified components of the boundary velocity in the radial and meridional directions. It can be seen

from the abovementioned treatment that the boundary value of the discrete pressure is unnecessary in these coordinates. Now, we substitute these relations into Eq. (3.4c) and find

$$A_{-1}(2, k) = 0, \quad C_{-1}(2) = 0$$

subsequently. It is also true for

$$A_{+1}(N_r - 1, k) = 0, \quad C_{+1}(N_\theta - 1) = 0$$

in which N_r and N_θ are the grid numbers in the radial and meridional directions. These result in two tridiagonal matrices in the radial and meridional directions. For the circumferential direction, it can be seen from the discrete equation, (3.4b), that a cyclic tridiagonal matrix is formed as periodicity of the pressure is imposed. So, we can compute the discrete pressure, first, by application of ADI (alternating-direction implicit) method (Peaceman and Rachford [14]) to the discrete pressure equation (3.4b), and then solving the system with a standard TDMA method for the two tridiagonal matrices and with a refined TDMA method (Temperton [15]) for the cyclic tridiagonal matrix.

3.5. *Overall Numerical Computation Procedure*

The overall numerical computation procedure to solve the time-dependent incompressible Navier–Stokes equations is as follows:

1. Solve the intermediate velocity $\acute{\mathbf{u}}$ from Eq. (3.2e);
2. Solve the intermediate velocity $\grave{\mathbf{u}}$ from Eq. (3.2f);
3. Solve the pressure p^{n+1} from Eq. (3.2i) with the divergence-free velocity equation (3.2h) satisfied;
4. Solve the velocity $\mathbf{u}^{n+1}$ from Eq. (3.2g), and then finish one time step calculation.

To complete the numerical method, adequate initial conditions of the velocity $\mathbf{u}^0$ and the pressure gradient $\mathbf{G}p^0$ are required. In the present study, we chose the Stokes solution as the initial velocity condition at $Re = 5$, i.e., $\mathbf{u}^0 = \mathbf{u}^0(0, 0, u^0_\phi)$ in which the Stokes flow profile is

$$u^0_\phi = \frac{1}{(1+\beta)^3 - 1}\left(-r + \frac{(1+\beta)^3}{r^2}\right)\sin\theta, \tag{3.5}$$

where the clearance ratio β is defined as $\beta = (R_2 - R_1)/R_1$. This Stokes flow is the time-independent, axisymmetric solution to Eqs. (2.3)–(2.6) and the boundary condition (2.7) in the limit $Re \to 0$. For the initial pressure gradient it can be found that $\mathbf{G}p^0 = 0$ is exactly satisfied in this Stokes solution of the spherical Couette flow. When considering a steady, low Reynolds number flow as the initial state, we generally have the relation $\mathbf{G}P^0 = \nabla^2\mathbf{u}^0/Re$ for the initial pressure condition.

In the following calculation, the computational domain is divided by a number of grids $22 * 361 * 91$ in the radial, meridional, and circumferential directions, respectively. The grids were constructed uniformly in the meridional and circumferential directions, while a geometric distribution was used in the radial direction in order to improve the resolution in the near-wall region of the spheres. The computational mesh in a meridional plane of the three-dimensional spherical shell is schematically shown in Fig. 3.

Since the viscous stability limit is removed by treating the conservative part of the viscous terms implicitly, the stability of the overall numerical method is restricted by the CFL condition. The local CFL number is defined as

$$\mathrm{CFL} = \left(\frac{|u_r|}{\Delta r} + \frac{|u_\theta|}{r\Delta\theta} + \frac{|u_\phi|}{r\sin\theta\Delta\phi} \right) \Delta t,$$

where Δr, $r\Delta\theta$, and $r\sin\theta\Delta\phi$ are the grid spacing of the spherical polar coordinates. The time increment Δt is then required for the restricted stability condition of $\max\{\mathrm{CFL}\} < 1$, where $\max\{\mathrm{CFL}\}$ is the maximum value of CFL number evaluated in the computational domain. However, the condition of $\max\{\mathrm{CFL}\} < 1$ here is only a guess, but not a known stability limit.

In the next section, we present the direct numerical simulation results in the case of $\beta = 0.14$. For comparison β has been chosen the same as that in the experiments (Nakabayashi [16], Nakabayashi and Tsuchida [17]). The Reynolds number was quasi-statically increased ($dR^*/dt = 0.0006$, R^* is defined as $R^* = \mathrm{Re}/\mathrm{Rec}$ in which Rec is the critical Reynolds number for occurrence of the Taylor–Görtler(TG) vortex) in order to eliminate the effect of the rotative acceleration ratio on the spherical Couette flow (Nakabayashi and Tsuchida [18]). Time integration was carried out until the steady or time-periodic state was obtained.

4. NUMERICAL RESULTS

4.1. *Axisymmetric 0-Vortex Flow, 0-Vortex Flow with Pinch and 1-Vortex Flow*

As the Reynolds number is increased from the initial value ($\mathrm{Re} = 5.0$) but still sufficiently low, we obtained numerical solutions which have been referred to as the 0-vortex flow (Marcus and Tuckerman [19]). The laminar subcritical regime of the spherical Couette flow is the combination of a primary azimuthal motion (axisymmetric) and a large-scale meridional circulation present on either side of the equator. Figures 6(a) and (b) show a typical numerical solution of the 0-vortex flow in meridional plane in the case of $\mathrm{Re} = 600$: (a) for the meridional streamline; (b) for azimuthal angular velocity. In the figures the intervals of the tick marks on the outer sphere denote the circumferential distance as β. The tick marks along the inner sphere are spaced at intervals of $\pi/18$ radians. For clarity, the gap width of the two spheres has been exaggerated by doubling from the interval $[1, 1+\beta]$ to $[1, 2(1+\beta)]$. Solid contours of the streamline denote counterclockwise circulation while those showing clockwise circulation are dashed. It can be seen from Fig. 6(a) that at $\mathrm{Re} = 600$ the meridional part of the basic flow consists of one large basic vortex in each hemisphere. The large basic vortices, which were first introduced by Marcus and Tuckerman [19], rotate in opposite directions in such way that the flow at the equator is directed from the inner sphere to the outer one. The dashed streamline located exactly at the equator is the outflow boundary between the two large vortices. As these vortices are easily confused with the Taylor–Görtler vortices which occur at high Reynolds number, we refer to it as the secondary flow circulation in this paper. Figure 6(b) depicts the contours of constant azimuthal angular velocity, $u_\phi/r\sin\theta$, for the flow in Fig. 6(a). The azimuthal angular velocity decreases from the inner to the outer sphere. The contours of the constant azimuthal angular velocity are parallel to the spherical boundaries, so we found that even at $\mathrm{Re} = 600$ the azimuthal angular velocity of the basic flow is a good approximation to that of the Stokes flow (Eq. (3.5)).

When the Reynolds number Re is increased to 900, the secondary flow circulations seem still qualitatively unchanged (comparing Fig. 6(c) with Fig 6(a)) while small wiggles of

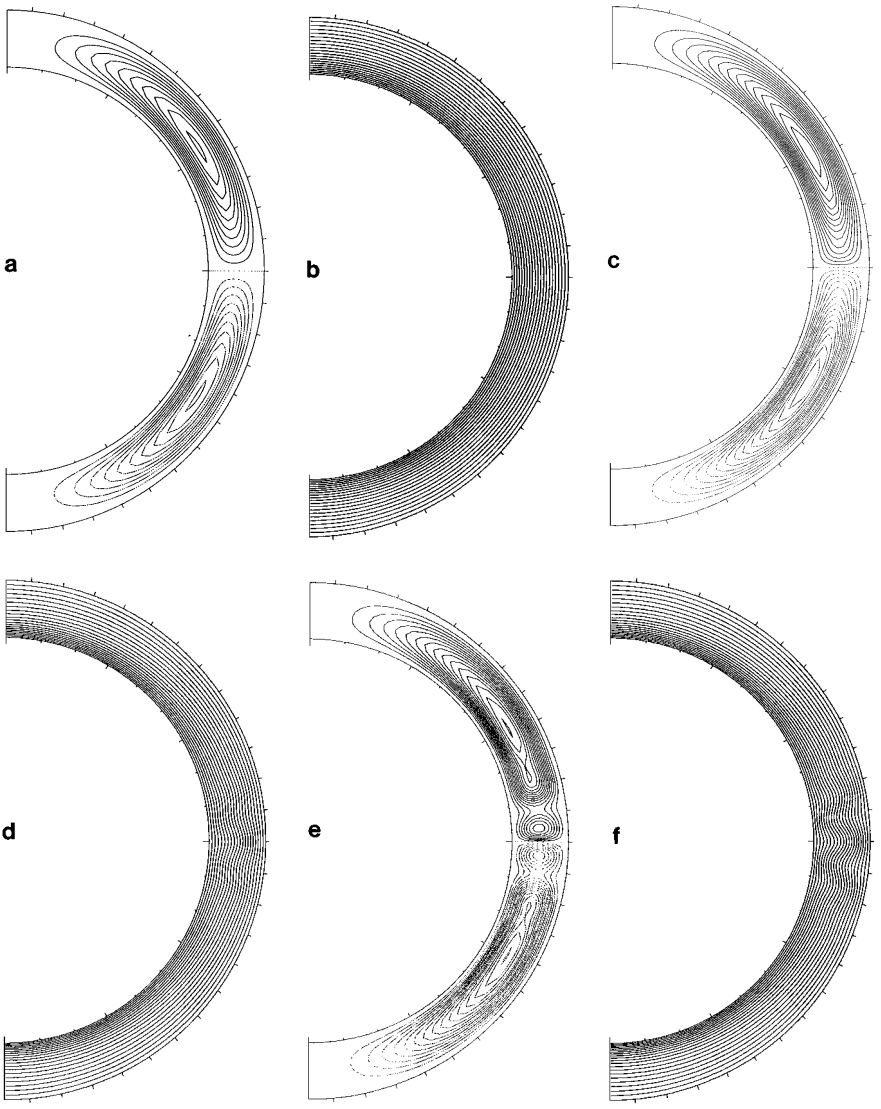

FIG. 6. (a), (c), (e), (g) contours of the meridional streamlines (solid lines, counterclockwise; dotted lines, clockwise). (b), (d), (f), (h) contours of the angular velocity on meridional plane (r, θ) for the axisymmetric spherical Couette flow at different Reynolds number Re $= 600, 900, 920$, and 940, respectively. The circumferential distance between the tick marks on the outer sphere is β. The tick marks on the inner sphere are spaced at intervals of $\pi/18$ radians. The gap width has been exaggerated to double from the interval $[1, 1+\beta]$ to $[1, 2(1+\beta)]$. Notice that these flows are equatorially reflection-symmetric.

contours of the azimuthal angular velocity appear near the equator (seen in Fig. 6(d)). This is because that the secondary flow begins to affect the distribution of the angular momentum.

At Re $= 920$ the basic flow is distorted slightly and the 0-vortex flow with pinches is formed. The pinching phenomenon of the 0-vortex flow is illustrated in Fig. 6(e). It is observed that there are two local maxima in the stream function in each hemisphere. The pinch is located about one gap width away from either side of the equator and is characterized by a stagnation point. The small circulation in closed streamlines near the either side of the equator has the same sign as that of the secondary flow circulation. As this circulation is

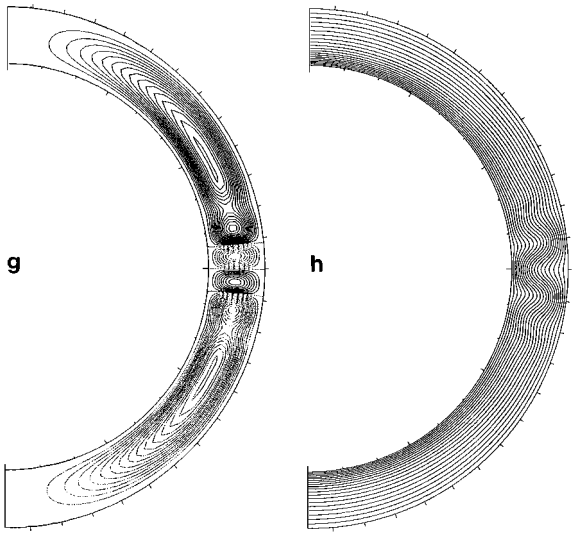

FIG. 6—*Continued*

not separated from the secondary flow circulation, it is usually not easily observed in an experiment. Figure 6(f) shows the azimuthal angular velocity contours of the pinched 0-vortex flow in Fig. 6(e). It is noted that the wiggles at the equator have increased in amplitude (compared with Fig. 6(d)). The secondary flow has developed strongly enough to affect the distribution of angular momentum between the spheres. Such a pinching phenomenon has been investigated numerically by Marcus and Tuckerman [19], Bar-Yoseph *et al.*[20], Dumas and Leonaed [9], and Zikannov [10].

As the Reynolds number Re is increased further (such that for $\mathrm{Re} \geq \mathrm{Rec}$ the critical Reynolds number for the first instability), the spherical Couette flow, like the circular Couette flow in rotating cylinders, will lose its stability. That is, at $\mathrm{Re} = \mathrm{Rec}$ the Taylor-type first instability occurs in the spherical Couette flow, and this first instability induces a transition from the basic flow into toroidal Taylor–Görtler (TG) vortices which are formed in the equatorial region. Figures 6(g) and (h) show our numerical solution of the 1-vortex flow at $\mathrm{Rec} = 940$ ($\mathrm{R}^* = 1$). It can be seen from the meridional streamlines of Fig. 6(g) that in each hemisphere there is one toroidal TG vortex near the equator with a diameter which is approximately equal to the gap width. The toroidal TG vortices are separated from the secondary flow circulation by a nearly straight streamline that extends from the inner sphere to the outer sphere. This streamline is an outflow ($\mathrm{u_r} > 0$) boundary between the toroidal TG vortex and the secondary flow circulation. At the equator there is an inflow ($\mathrm{u_r} < 0$) boundary between the two toroidal TG vortices. The circulation of the toroidal TG vortex has an opposite sign to that of the secondary flow. We found in our numerical simulation that the critical Reynolds number $\mathrm{Rec} = 940$ ($\mathrm{R}^* = 1$) for onset of the toroidal TG vortices is close to 900, the one obtained in the experiments (Nakabayashi [16], Nakabayashi and Tsuchida [17]) (see Table 1). Figure 6(h) shows that the wiggles of the contours of the azimuthal velocity are more pronounced than those of the 0-vortex flow with pinch in Fig. 6(f), and it means that there is much angular momentum transfer occurring in the 1-vortex flow than that in the pinched 0-vortex flow. The distortions of the azimuthal velocity contours, which are opposite in sign to those in the 0-vortex flow with pinch, are due to the toroidal TG vortices.

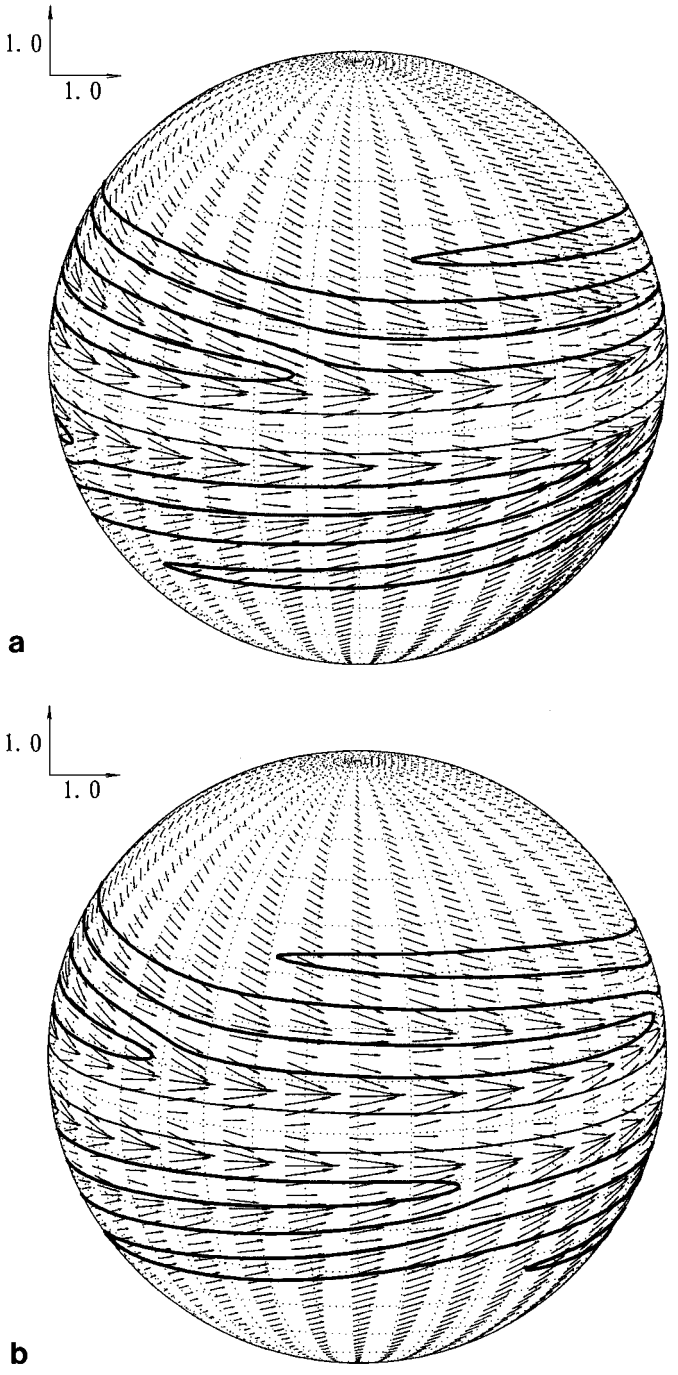

FIG. 7. Plots of the velocity vectors of the spiral TG vortex flow in the (θ, ϕ) spherical cross section at mid-gap radius viewed from (a) $\phi = \pi/2 - 2\pi/9$, (b) $\phi = \pi - 2\pi/9$, (c) $\phi = 3\pi/2 - 2\pi/9$, (d) $\phi = 2\pi - 2\pi/9$. The Reynolds number for occurrence of these spiral TG vortices Res is 1100 in the numerical simulation. Contour of the zero radial velocity ($u_r = 0$) on this section is also drawn with two types of solid lines. Thin solid lines indicate the center positions of the two toroidal TG vortex cells. The thick ones, which are counted by every two thick lines from each side of the equator, correspond to the center lines of the spiral TG vortex.

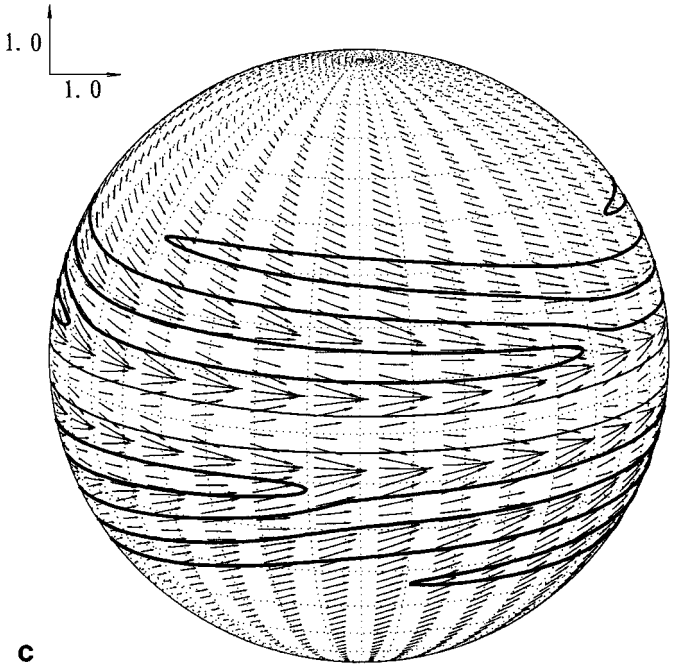

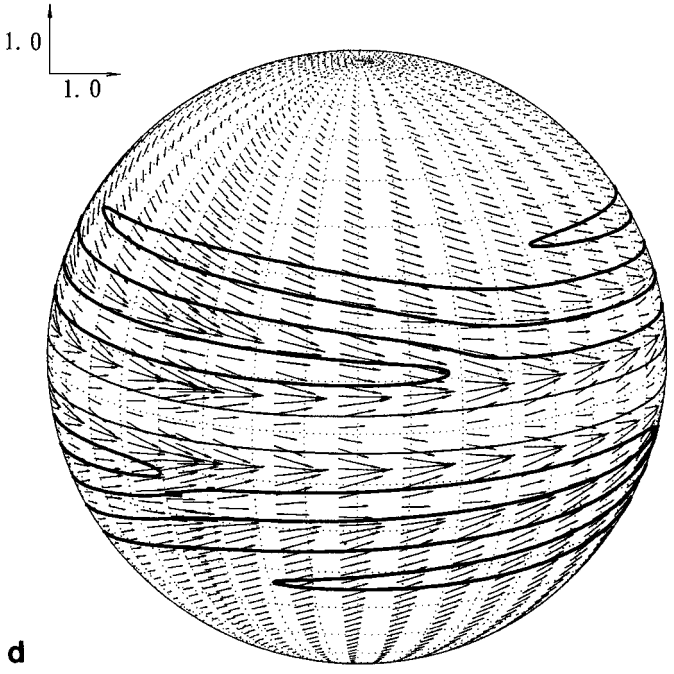

FIG. 7—*Continued*

TABLE 1
Comparison between the Numerical Simulation and the Experimental Results

	Toroidal TG vortex		Spiral TG vortex	
	Dynamical characteristics	Geometrical characteristics	Dynamical characteristics	Geometrical characteristics
Experiments[16],[17]	$R^* = 1$(Rec = 900) Steady	Axisymmetric Equal widths to clearance	$R^* = 1.13$ (Res = 1017) Move in rotating direction	Three pair of spirals No-equatorial symmetry
Present study	$R^* = 1$ (Rec = 940) Steady	Axisymmetric Equal widths to clearance	$R^* = 1.18$ (Res = 1110) Move in rotating direction	Three pair of spirals No-equatorial symmetry

Our numerical solutions of the 0-vortex flow, the 0-vortex flow with pinch and the 1-vortex flow mentioned above are found to be in close similarity in qualitative features to the flows in other numerical work (Marcus and Tuckerman [19]). A more detailed comparison of the computed toroidal TG vortices with the ones observed in the experiments (Nakabayashi [16], Nakabayashi and Tsuchida [17]) shows a good agreement in quantitative features (see Table 1).

4.2. *Three-Dimensional Spiral TG Vortex Flow*

In this subsection, we present the results on the numerical simulation of the so-called spiral Taylor–Görtler (TG) vortex (Nakabayashi [16]). Dumas and Leonaed [9] have been successful in simulation of the three-dimensional spiral TG vortices for a narrow gap case ($\beta = 0.06$). In this numerical simulation, we are concerned with $\beta = 0.14$, a moderate gap case.

As we raise the Reynolds number Re to a higher value, the 1-vortex flow becomes unstable due to the secondary instability, and its symmetry is broken. This secondary instability results in a transition from the 1-vortex flow to the supercritical spiral TG vortex flow. This three-dimensional spiral TG vortex flow at Re = Res = 1110 (Res: the Reynolds number for occurrence of the spiral TG vortex) is illustrated in the following Fig. 7 and Fig. 8. First, Fig. 7 shows the plots of the velocity vectors (u_ϕ, u_θ) of the spiral TG vortex flow in the (θ, ϕ) spherical cross section at mid-gap radius viewed from (a) $\phi = \pi/2 - 2\pi/9$, (b) $\phi = \pi - 2\pi/9$, (c) $\phi = 3\pi/2 - 2\pi/9$, (d) $\phi = 2\pi - 2\pi/9$. The flow on the section moves in the same direction as that of the inner rotating sphere (counterclockwise). The contour of the zero radial velocity ($u_r = 0$) in this section is also drawn with two types of solid lines, which is the boundary between existing inflow ($u_r < 0$) and outflow ($u_r > 0$). Thin solid lines indicate the center positions of the two toroidal TG vortices. The thick ones, which are counted by every two thick lines from each side of the equator, correspond to the center lines of the spiral TG vortices. Figure 8 gives the bird's-eye view of the radial velocity (u_r) in the same spherical cross section as that in Fig. 7. To compare it with the same contour line in the Fig. 7, the zero contour of the radial velocity ($u_r = 0$) is also projected onto the (θ, ϕ) plane. It is observed in Figs. 7 and 8 that there is one toroidal TG vortex and three spiral TG vortices in each hemisphere. The three pairs of the spiral TG vortices are formed on each side of the one pair of the toroidal TG vortices. The lines of the center positions of the toroidal TG vortices(or say the axes of the TG toroidal vortices) are nearly parallel to the equator while the center lines of the spiral TG vortices (or say the axes of the spiral

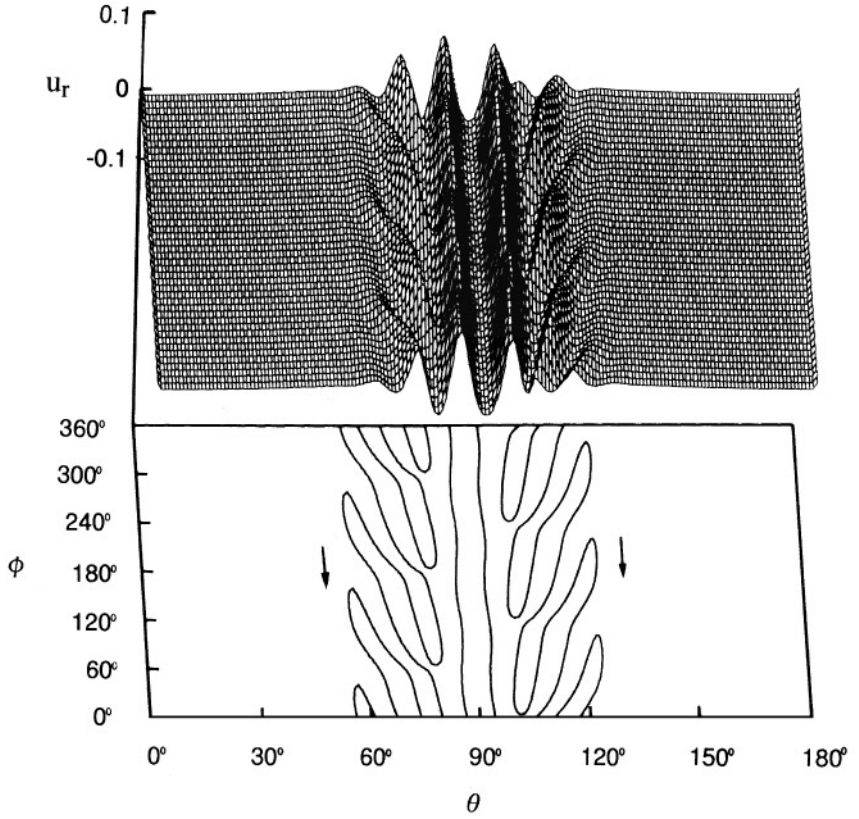

FIG. 8. Bird's-eye view of the radial velocity in the same spherical cross section as that in Fig. 7, but shown in Cartesian coordinates. For comparison with Fig. 7, the zero contour of the radial velocity ($u_r = 0$) is also projected onto the (θ, ϕ) plane. Arrows show the direction of the spiral TG vortices's movement.

TG vortices) are tilted with respect to the azimuthal direction. Obviously, the spiral TG vortices are equatorially asymmetric and travel in the azimuthal direction (the same as the inner rotating sphere). The arrows in Fig. 8 show the direction of the spiral TG vortices's movement. Table 1 also displays the characteristics of the spiral TG vortices simulated with the numerical method and the ones of the experiments (Nakabayashi [16] and Nakabayashi and Tsuchida [17]). Quantitatively, the numerical simulation on the spiral TG vortices gives a good agreement with the experiments.

5. SUMMARY

A finite-difference method for solving three-dimensional, time-dependent incompressible Navier–Stokes equations in spherical polar coordinates is presented in detail. A new algorithm, which is second-order accurate in time and space, is considered, and decoupling between the velocity and the pressure is achieved by this algorithm. A staggered grid system is used in the present study, so the treatment of singularities of the equations in spherical polar coordinates is avoided. The discrete velocity equations are solved with the approximate factorization technique and standard TDMA method, while the discrete Poisson equation is solved with the ADI technique and a refined TDMA method.

Further, the numerical method is tested by computing the spherical Couette flow between two concentric spheres with the inner one rotating. We simulated the subcritical flows (0-vortex flow, 0-vortex flow with pinch) and the supercritical flows (TG vortex flow, spiral TG vortex flow). A comparison of the numerical solutions with available numerical results and experimental measurements was made. It is demonstrated that the initial-boundary numerical code is valid for solving three-dimensional, unsteady incompressible Navier–Stokes equations in spherical polar coordinates.

ACKNOWLEDGMENTS

The research was supported by Grants-in-Aid for Scientific Research No. 08650198 form the Ministry of Education, Science, and Culture, Japan. The computations were carried out with NEC supercomputer (SX4) at the computing center of the National Institute for Environmental Studies, Japan.

REFERENCES

1. A. J. Chorin, *Math. Comput.* **22**, 745 (1968).
2. J. Kim and P. Moin, *J. Comput. Phys.* **59**, 308 (1985).
3. J. Van Kan, *SIAM J. Sci. Statist. Comput.* **7**, 870 (1986).
4. J. B. Bell, P. Colella, and H. M. Glaz, *J. Comput. Phys.* **85**, 257 (1989).
5. P. M. Gresho, *Int. J. Numer. Methods Fluids* **11**, 587 (1990).
6. J. K. Dukowicz and A. S. Dvinsky, *J. Comput. Phys.* **102**, 336 (1992).
7. J. B. Perot, *J. Comput. Phys.* **108**, 51 (1993).
8. J. B. Perot, *J. Comput. Phys.* **121**, 190 (1995).
9. G. Dumas and A. Leonard, *J. Comput. Phys.* **111**, 205 (1992).
10. O. Y. Zikanov, *J. Fluid Mech.* **310**, 293 (1996).
11. R. M. Beam and R. F. Warming, *J. Comput. Phys.* **22**, 87 (1976).
12. W. R. Briley and H. McDonald, *J. Comput. Phys.* **24**, 372 (1977).
13. F. H. Harlow and J. E. Welch, *Phys. Fluids* **8**, 2182 (1965).
14. D. W. Peaceman and H. H. Rachford, *J. Soc. Indust. Appl. Math.* **3**, 28 (1955).
15. C. J. Temperton, *J. Comput. Phys.* **19**, 317 (1975).
16. K. Nakabayashi, *J. Fluid Mech.* **132**, 209 (1983).
17. K. Nakabayashi and Y. Tsuchida, *J. Fluid Mech.* **194**, 101 (1988).
18. K. Nakabayashi and Y. Tsuchida, *J. Fluid Mech.* **295**, 43 (1995).
19. P. S. Marcus and L. S. Tuckerman, *J. Fluid Mech.* **185**, 1 (1987).
20. P. Bar-Yoseph, *Phys. Fluids A* **2**, 1564 (1990).